

Benchmarking the reproducibility of all-solid-state battery cell performance

Received: 30 April 2024

Accepted: 15 August 2024

Published online: 18 September 2024

Check for updates

Sebastian Puls¹, Elina Nazmutdinova^{2,3}, Fariza Kalyk¹, Henry M. Woolley^{3,4}, Jesper Frost Thomsen^{3,5}, Zhu Cheng⁶, Adrien Fauchier-Magnan⁷, Ajay Gautam⁶, Michael Gockeln⁸, So-Yeon Ham⁹, Md Toukir Hasan¹⁰, Min-Gi Jeong¹¹, Daiki Hiraoka¹², Jong Seok Kim¹³, Tobias Kutsch^{14,15}, Barthélemy Lelotte¹⁶, Philip Minnmann¹⁷, Vanessa Miß¹⁸, Kota Motohashi¹², Douglas Lars Nelson¹⁹, Frans Ooms⁶, Francesco Piccolo^{20,21}, Christian Plank^{22,23}, Maria Rosner^{24,25}, Stephanie E. Sandoval^{19,26}, Eva Schlautmann², Robin Schuster^{14,15}, Dominic Spencer-Jolly^{27,28}, Yipeng Sun²⁹, Bairav S. Vishnugopi¹⁰, Ruizhuo Zhang³⁰, Huang Zheng³¹, Philipp Adelhelm^{20,21}, Torsten Brezesinski³⁰, Peter G. Bruce^{27,32}, Michael Danzer^{22,23}, Mario El Kazzi¹⁶, Hubert Gasteiger¹⁴, Kelsey B. Hatzell¹¹, Akitoshi Hayashi¹², Felix Hippauf²⁴, Jürgen Janek¹⁷, Yoon Seok Jung¹³, Matthew T. McDowell^{19,26}, Ying Shirley Meng^{33,34}, Partha P. Mukherjee¹⁰, Saneyuki Ohno^{31,35}, Bernhard Roling¹⁸, Atsushi Sakuda¹², Julian Schwenzel⁸, Xueliang Sun²⁹, Claire Villevieille⁷, Marnix Wagemaker⁶, Wolfgang G. Zeier^{1,2} & Nella M. Vargas-Barbosa^{1,23,36} ✉

The interlaboratory comparability and reproducibility of all-solid-state battery cell cycling performance are poorly understood due to the lack of standardized set-ups and assembly parameters. This study quantifies the extent of this variability by providing commercially sourced battery materials—LiNi_{0.6}Mn_{0.2}Co_{0.2}O₂ for the positive electrode, Li₆PS₅Cl as the solid electrolyte and indium for the negative electrode—to 21 research groups. Each group was asked to use their own cell assembly protocol but follow a specific electrochemical protocol. The results show large variability in assembly and electrochemical performance, including differences in processing pressures, pressing durations and In-to-Li ratios. Despite this, an initial open circuit voltage of 2.5 and 2.7 V vs Li⁺/Li is a good predictor of successful cycling for cells using these electroactive materials. We suggest a set of parameters for reporting all-solid-state battery cycling results and advocate for reporting data in triplicate.

As the field of all-solid-state batteries (ASSBs) continues to develop, both academically and commercially, the necessity for performance benchmarking increases¹. Although recent reports demonstrate the viability of producing solid-state pouch cells^{2,3}, the majority of ASSB reports rely on measurements from press cells. These consist of a solid electrolyte (SE) separator (about 500 µm thick) sandwiched between the active materials, all of which are then pressed between two metal stamps. Typically, an outer frame or screws adjust and maintain a

certain cell pressure (sometimes referred to as the stack pressure, in the range of 5–400 MPa) during cycling. To date, there is no standardized ASSB cell set-up available; multiple custom set-ups are in use but not commercially available.

Unsurprisingly, this lack of standardization leads to severe reproducibility issues. For example, ASSB cells with LiNi_{0.6}Mn_{0.2}Co_{0.2}O₂ (NMC 622) as positive electroactive material (in literature often referred to as cathode active material, CAM), a lithium chloride argyrodite

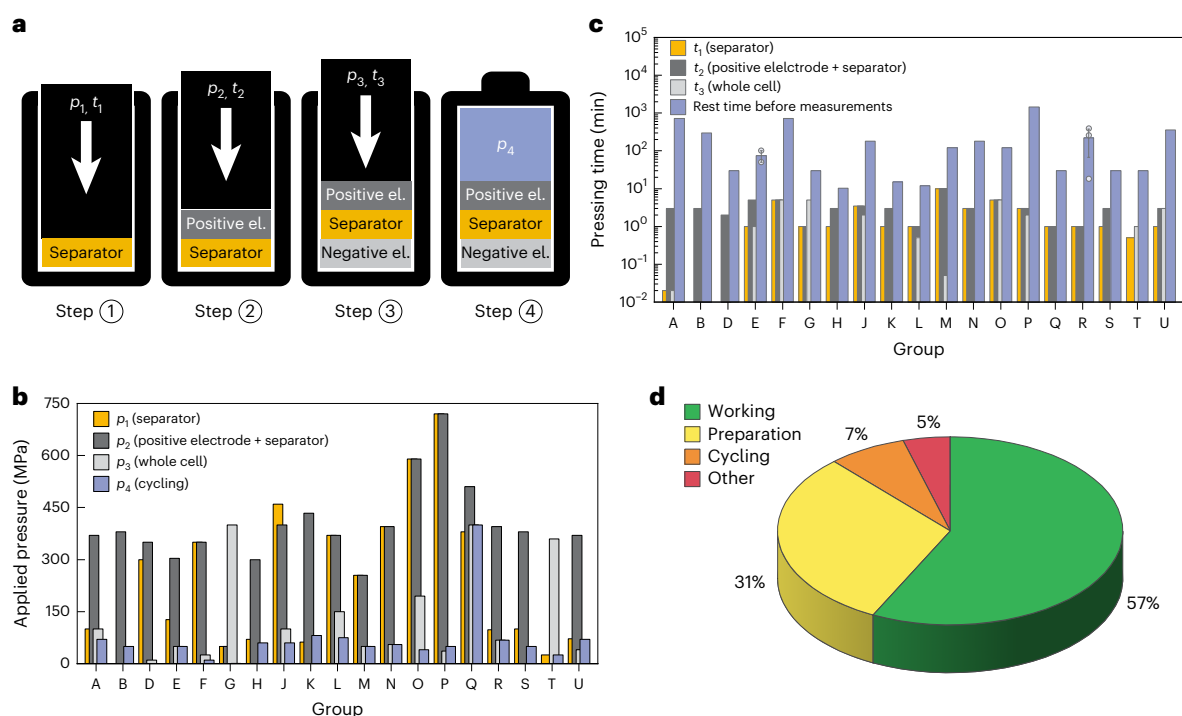


Fig. 1 | Cell assembly protocol, assembly conditions and failure rate.

a, Schematic workflow for the stepwise assembly of an ASSB press cell. Here p_x and t_x correspond to the applied uniaxial pressure and duration of the compression at each step, respectively. el., electrode. **b, c**, Uniaxial pressures p_x applied (**b**) and duration t_x (**c**) of the pressing step during the preparation of the different cell components and cell cycling. For all cells built by one group, the same assembly pressures and times were used, except for groups E and R where

rest times before OCV measurement differ for their two and three working cells, respectively. The specific rest times for these cells are shown by filled dots, and the error bars mark the standard deviation of these values. If no value is shown for a group, no pressure or time was applied for that step. **d**, Number of the attempted ASSB cells working and failed in this study. For the cells that failed, the reason of the failure is shown. Cells cycled up to the 50th cycle at 0.1 C are considered as working cells.

($\text{Li}_6\text{PS}_5\text{Cl}$) SE separator and $\text{In}/(\text{InLi})_x$ as a negative electrode show initial specific discharge capacities between 106 and 142 mAh g^{-1} at a C rate of 0.1 C and up to 157 mAh g^{-1} when a conductive carbon was added to the positive electrode composite (often referred to as cathode composite, CC)^{4–10}. Moreover, the capacity retention and cell impedance evolution are drastically different, which makes a direct comparison of the various reports challenging. Differences in material coatings, morphologies, loadings, CC compositions, cycling procedures, temperatures and cell set-ups contribute to these disparities. Additionally, the processing conditions used in the literature differ; including compression pressures of the cell components and cycling pressures, both influencing the cycling properties¹¹. All the above-mentioned aspects challenge interlaboratory comparability of the electrochemical performance of ASSB cells, even when using the same materials.

In this Article we report on the interlaboratory reproducibility of ASSB cell performance based on a dataset contributed by 21 groups previously reporting independent work on ASSBs. Each group was provided the same battery materials: single crystal NMC 622 as CAM, $\text{Li}_6\text{PS}_5\text{Cl}$ powder as SE and indium foil. The groups were asked to assemble up to three cells with the following specifications. First, a positive composite electrode was made with a ratio of $m(\text{CAM}):m(\text{SE}) = 70:30$ (no additives, hand ground) and an areal CAM loading of 10 mg cm^{-2} . Second, a separator was used with an areal loading of about 70 mg cm^{-2} . Third, an alloy negative electrode was made using the provided indium foil and their own sourced Li metal. A typical assembly workflow is shown in Fig. 1a. Note that each group was asked to use their individual cell set-up and their own processing protocol to assemble the cells. Therefore, different pressures were used during assembly and cycling (Supplementary Table 1). After assembly, each group was asked to follow the same cycling protocol (Methods) to provide details about their

cell assembly protocol and to share their raw electrochemical data. The data analysis was performed by the coordinating group to minimize variability sources in the results¹².

Variability of cell assembly conditions

The assembly of ASSB cells, hereafter simply referred to as cells, is a multi-step process in which uniaxial compression is applied to ensure good interparticle contact between the various cell components (Fig. 1a). Briefly, in the first step, the separator is compressed; then, the positive composite electrode is distributed on top of the pressed separator for further compression; subsequently, the alloy for the negative electrode is added to the other side of the separator for further compression and fixing the stack pressure (cycling pressure) of the cell. The variability of the pressing conditions among the groups is shown in Fig. 1b. Although the applied pressure at each step is not consistent among groups, the average cycling pressure is mostly in the range of 10–70 MPa, and the average pressures used to compress the positive composite electrode range from 250–520 MPa.

Larger variabilities (several orders of magnitude difference) are reported for the duration of each compression step (Fig. 1c). The latter has been shown to play a crucial role in the resulting ionic conductivity of sulfide-based solid electrolytes^{13,14}. Indeed, high pressure (>300 MPa) and long compression times (in the order of several hours) are required to densify and reduce residual void space in thiophosphate-based SEs that enable higher ionic conductivities. However, NMC (secondary) particles are prone to breaking at such pressures, especially when compressed for extended periods of time¹⁵.

Despite the variability in the processing conditions, the reported thicknesses of all cells are similar (Supplementary Tables 2–20), showing again that the processing protocol mostly plays a role in the

resulting microstructure of each battery, which strongly affects its electrochemical performance⁶. Note that the specific compression profiles, including how fast the pressure is applied and released, and the way the pressure was controlled (if it was controlled at all; Supplementary Table 1), was not monitored in this study but is expected to have an effect on the microstructure.

Of the total 68 cells attempted, 39 (57%) were cycling to the 50th cycle. These cells are listed as *working* in the statistics (Fig. 1d). The number of non-working cells is generally not reported in the literature. In this study, the most common reason for failure (21 batteries, 31%) is preparation. Examples of these preparation issues are broken pellets, inhomogeneous distribution of the positive composite electrode on the separator layer or elevated water and moisture levels in the inert atmosphere of the glovebox. A total of 5 batteries (7%) failed during cycling, for example due to short circuiting. A smaller number (3 batteries, <5%) has other reasons for failure that are not related to preparation or the cell chemistry, for example, accidentally unplugging a cell during cycling. These reasons are referred to as *human errors*. Thus, the preparation and handling of ASSB cells is challenging and results in a high failure rate (although seldom reported). However, once a cell attains some initial capacity, cycling it up to 50 cycles is not very problematic. Note that due to the large number of failed batteries, some groups in this work reported fewer than the targeted number of three batteries, because each group received enough material for three to four cells.

Variability of initial open circuit voltage

Before constant current cycling, the open circuit voltage (OCV) of each cell was measured. The OCV is the thermodynamic voltage of the cell and is defined by the cell chemistry. The difference in the electrochemical potentials of the electrons in the positive and negative active materials defines the OCV; therefore, the OCV also depends on the state of charge of a cell^{17–19}. To benchmark the NMC material for this study and obtain a better estimate of the starting OCV for the ASSBs, Li-ion battery (LIB) coin cells using NMC 622, Li metal and 1 M LiPF₆ in V(EC):V(EMC) = 3:7 as liquid electrolyte were assembled (detailed information about the materials and cathode preparation procedures are in the Methods section). The LIBs show an OCV of 2.8 ± 0.2 V vs Li⁺/Li (number of cells, $n_{\text{LIB}} = 3$), immediately after assembly. After 5 h of rest, the OCV of the cells increases to 3.0 ± 0.1 V vs Li⁺/Li. The increase over time and stabilization of the OCV in LIBs is explained by the formation of interphases at the surface of the electroactive material particles and wetting effects²⁰.

In the case of the ASSBs, all voltages were measured against the lithium–indium alloy negative electrode. Therefore, to make the OCV values comparable to other systems, they were converted to values vs Li⁺/Li assuming $E(\text{Li}^+/\text{Li}) = E(\text{Li}^+/\text{In}-(\text{InLi})_x) + 0.62$ V (ref. 21). Fig. 2a shows a violin plot summarizing the OCVs of all cells prepared. The box corresponds to the interquartile range (IQR) of the data, the whiskers represent $1.5 \times$ IQR, and any data points outside this range are considered a statistical outlier. Although the initial OCV of the ASSB cells was not measured after a pre-determined equilibration time, most values are within the OCV range of the liquid cells measured directly after assembly (about 2.64 to 3.02 V vs Li⁺/Li), although closer to the lower end of that range and at least 0.05 V lower than the OCVs of the LIBs measured after the 5 h rest. As with the liquid cells, time is required for a stable OCV in the ASSB cells, and additionally, to the interfacial formation effects, the OCV could be influenced by the pressure relaxation, which is observed in ASSB cells after compression²². On the basis of Fig. 2a, due to their very low initial OCV, five cells are considered to be outliers and are excluded from all further statistical analyses and box plots. Specifically, the cells taken out due to their low OCV are groups A (both cells), F (both cells) and G (one of three cells). Moreover, group J (reported only one cell) is removed from all statistics because their cell was cycled in the wrong potential window. Once these outliers are removed, we calculate an average OCV for all ASSB cells of 2.6 ± 0.1 V vs

Li⁺/Li, even though each group used their own lithium metal to prepare the alloy negative electrode, their individual alloy preparation method, a variable atomic ratio of lithium to indium among the cells and measured the OCV at different resting times before OCV measurement and cycling. The In-to-Li atomic ratios of the cells range from 1.33:1 to 6.61:1, except for group N with 0.77:1 (Supplementary Table 21 includes all values). The median atomic ratio among all groups is 2.48:1. Thus, the alloy in all cells, except those of group N, starts in the two-phase region (In + InLi) of the In–Li phase diagram²¹, but even the deviating group shows reasonable initial OCVs. However, as Li⁺ ions are moving from the positive electrode to the alloy negative electrode during the first charge, the additional Li⁺ ions from the NMC could still lead to a shift to the lithium-rich regions in the In–Li phase diagram, where Li-rich In–Li alloy phases with lower potentials vs Li⁺/Li are present. This can cause an incomplete deintercalation of Li⁺ from the positive electroactive material and consequently lower specific capacities. The latter is observed for group N (for example 48.6 mAh g⁻¹ at the first 0.1 C discharge cycle; Supplementary Fig. 1).

Once the OCV of the cells was determined, symmetric constant current charge/discharge cycling was performed. It started with two formation cycles at 0.05 C, in the following referred to as *pretreatment cycles*, followed by 50 cycles at 0.1 C. Impedance measurements were performed in the charged and discharged state in the first and second pretreatment cycle and after 50 0.1 C cycles. The pretreatment data was provided by only 11 ($n_{\text{ASSB,pretreatment}} = 23$) out of the 21 groups. Therefore, it is not fully comparable to the dataset based on the cycling at 0.1 C (up to 50 cycles; $n_{\text{ASSB,0.1C}} = 33$). Note that the initial OCV was the only criterion used to exclude specific cells from further analyses; for all further box plots, new cells may be identified and shown as outliers in these specific box plots but are not sequentially removed. Figure 2b–d shows the violin plots of the initial specific (dis-)charge capacities at 0.05 C, first and 50th cycle specific discharge capacities at 0.1 C, Coulomb efficiencies and polarization voltages of the ASSB cells. The comparative values from the LIBs are shown as triangles. In general, the average and median for all these histograms are not close to one another, which demonstrates that these data do not conform to a normal distribution.

Cycling performance variability

Figure 2b shows the large scatter in the reported specific capacities of the cells, indicated by large IQRs. Regarding the pretreatment (0.05 C) cycles, most cells (59%) have specific capacities in the range between 170–195 mAh g⁻¹ and 130–155 mAh g⁻¹ during charge and discharge, respectively. The rest of the cells show much lower specific capacities, with the lowest specific charge and discharge capacities at 71 and 47 mAh g⁻¹. The average values are at least 15 mAh g⁻¹ lower compared with the median values, as they are strongly influenced by the low-capacity cells. Compared with the liquid cells, the highest specific charge capacities of ASSB cells are in the same range, whereas the highest specific discharge capacities are about 20 mAh g⁻¹ lower. The Coulomb efficiency of the ASSB cells in the pretreatment (0.05 C) is considerably less scattered than the specific capacities (Fig. 2c). It is lower for the ASSBs than for the LIBs, due to lower specific discharge capacities. Coulomb efficiencies in the first cycle are known to be lower compared with subsequent cycles as irreversible, parasitic surface reactions take place, including structural changes of the positive electroactive material²³. Except for four cells, the initial Coulomb efficiency is above 75%.

Regarding the 0.1 C cycling, the initial specific discharge capacities of the ASSB cells range from 21 to 143 mAh g⁻¹, with a median of 121.9 mAh g⁻¹ and an average of 103.7 mAh g⁻¹. The distribution appears somewhat bimodal, with approximately half of the cells having high initial capacities between 110 mAh g⁻¹ and 145 mAh g⁻¹, and a smaller cluster in the range of 60–80 mAh g⁻¹. On average, the initial capacity of the 0.1 C cycles decreases by about 16 mAh g⁻¹ compared with the

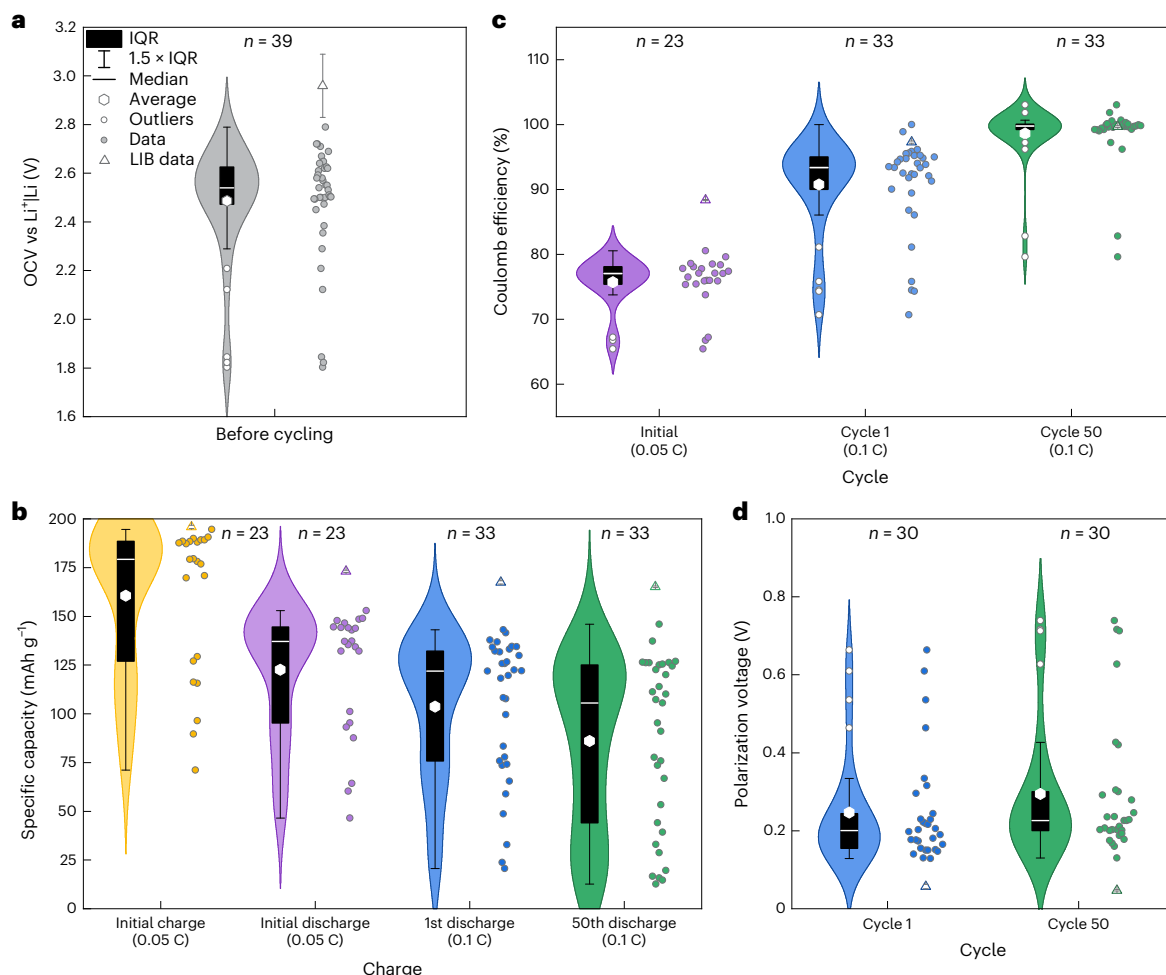


Fig. 2 | Analysis of various cell performance figures of merit. a–d, Violin plots showing the open circuit voltage (OCV) of all cells, measured after assembly, and converted to vs. Li^+/Li (a); specific (dis-)charge capacities of the pretreatment and 0.1 C cycling (b); Coulomb efficiencies (c) and polarization voltage (d), calculated from average charge minus average discharge voltage of the respective cycle. Boxes inside the violin diagrams show the IQR, whiskers extend

to 1.5 times of IQR. The number n of ASSB cells considered for the analysis is shown above each violin plot. All violin plots are prepared with Kernel density estimation. The triangles show the LIB coin cell data of three coin cells used to benchmark the NMC 622 active material, the error bars show their standard deviation (SD). Details on the preparation of these coin cells is provided in Methods.

second 0.05 C pretreatment capacity. This is, among other reasons, due to the limited rate capability known for ASSBs with $\text{Li}_6\text{PS}_5\text{Cl}$ solid electrolyte^{10,24}. The final specific discharge capacities in the 50th cycle are even more scattered than the initial ones, resulting in a larger interquartile range (between 44.2 and 125.3 mAh g^{-1}). In general, the final specific discharge capacities are lower than the initial ones, with both average and median decreasing by similar values of 18 mAh g^{-1} and 16 mAh g^{-1} , respectively. The Coulomb efficiency in the 50th cycle, depicted in Fig. 2c, is relatively high, with a median of 99.8% and an average of 98.6%. The groupwise cycling data, including the accumulated irreversible capacities, an indication for decomposition reactions and active lithium loss of cells, can be found in the Supplementary Figs. 2–5.

The capacity retention represents the ratio of the discharge capacities of the 50th and the first 0.1 C cycles (Supplementary Fig. 6). Most of the cells have retentions between 75% and 100%, median and average are 91.6% and 81.1%. On the one hand, five cells (H1, R1, R3, S1, S2) show retentions slightly higher than 100%, up to 107%, mainly due to an increase in the capacity during the first ten cycles, followed by stable cycling behaviour. On the other hand, three groups, namely D, F and G, found very low-capacity retentions (< 50%) and reported low cycling pressures between 1 and 10 MPa, if reported at all. The requirement for sufficient cycling pressure is known from the literature¹¹. The presented

data suggests that cycling pressures of >25 MPa are required for stable cycling in these types of cells. However, the cycling pressure seems to be less important for initial capacities, as suggested by the high-capacity cells D1 and F2. In other words, the initial capacity of the cells is mostly influenced by the processing of the materials during cell assembly, whereas the capacity retention of the cells requires high cycling pressures due to the volume changes of the materials during cycling. The capacity retention median of 91.6% and the small IQR demonstrate that even low-capacity cells retain their capacities and show stable cycling. The specific causes for the low-capacity cells are difficult to ascertain within the present study. However, experience suggests that inhomogeneous positive composite electrode mixing and distribution, which leads to a worse utilization of positive electroactive material during cycling and propagating weighing errors are the most likely causes. Finally, the atmosphere of the glovebox (for example, content of H_2O and O_2 , whether solvents are stored in it) might cause material degradation and reduce the cell performance. However, as all groups reported $\text{H}_2\text{O}/\text{O}_2$ content below 5 ppm, we do not see a direct correlation to cell performance.

The polarization voltage, sometimes also referred to as polarization growth or ΔV ^{25,26}, is calculated as the difference between the average charge voltage and the average discharge voltage of each cycle.

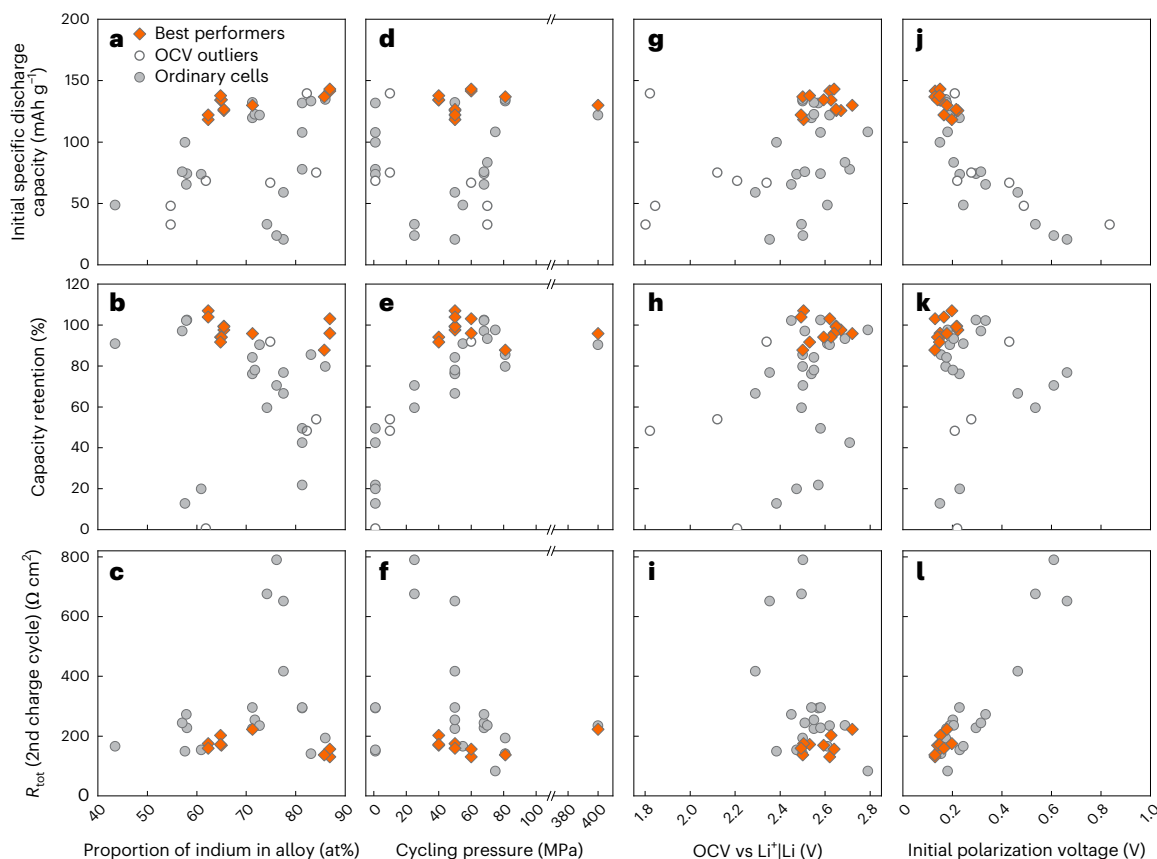


Fig. 3 | Correlations between various assembly and cycling parameters. **a–l**, Spread of the initial specific discharge capacities, the capacity retentions and the total cell resistances R_{tot} as a function of the indium content (atomic%) in the $\text{In}/(\text{InLi})_x$ alloy electrode (**a–c**), the cycling pressure (**d–f**), the initial OCV (**g–i**) and the initial polarization voltage (**j–l**). Outliers are shown as open circles,

best performer cells with final specific discharge capacities $>120 \text{ mAh g}^{-1}$ as filled diamonds and the remaining cells as filled circles. In (**d–f**) the x-axis break between 120 and 350 MPa was used for a better representation of the data as no groups reported cycling pressures in this range.

Figure 2d depicts the polarization voltage at the beginning and end of the cycling protocol. Note that the number n of cells considered for this statistic is 30, because voltages were not provided by group D. The differences between the absolute polarization voltages of the different cells are large. Most of the ASSB (69%) have low initial polarization voltages between 0.10 V and 0.25 V. The rest of the cells are scattered, up to an initial value of 0.7 V. Between the first and the 50th cycles, an increase in polarization voltage is observed. The median increases slightly by 30 mV from 0.20 V in cycle 1 to 0.23 V in cycle 50, whereas the average increases by 40 mV from 0.25 V to 0.29 V. This corresponds to the expected trend, as interfaces and interphases form during cycling, and the impedance of a cell is expected to increase with increasing number of cycles, thereby contributing to the cell's capacity fading²².

Cell processing parameters and performance correlations

The large differences in the electrochemical performances of ASSBs could, among other reasons, originate from the variation in the processing parameters used by the different groups. To find possible similarities and correlations between processing and performance, we define some cells as the *best performers*. As criteria for the *best performers*, we choose cells that retain specific discharge capacities $>120 \text{ mAh g}^{-1}$ after 50 cycles (Supplementary Fig. 7). This results in the following 12 cells: B1–B3, H1–H2, K2, O1–O3, Q1, and S1–S2. These cells are depicted with an orange diamond symbol in Fig. 3. Regarding their cycling performance, these best performers show initial OCVs $>2.5 \text{ V vs Li}^+/\text{Li}$, initial polarization voltages between 0.10 V and 0.25 V and capacity retentions $>85\%$.

Although the *best performer* cells are prepared differently, we identify four commonalities. First, the resistance of the separator (R_0 , extracted from distribution of relaxation times (DRT)-based impedance data analysis²⁷; Methods) ranges between 18 and $42 \text{ } \Omega \text{ cm}^2$ (Supplementary Fig. 8), even though the range of uniaxial pressures applied for preparing the separator range between ‘hand-pressing’ (group B) and 590 MPa (group O). Second, the separator together with the positive electrode composite of the *best performers* was compressed within the narrow(er) range between 300 and 590 MPa for times between 1 and 5 min. Third, the compression of the whole cell, namely CC + SE + $\text{In}/(\text{InLi})_x$, was not done by most of the *best performers* (four of six groups), and therefore it is unlikely that this step on its own plays a large role in the cycling performance. Fourth, even though we did not prescribe the cycling pressure, most groups chose to do the cycling at pressures $>40 \text{ MPa}$, showing a bias towards good cell performance and not necessarily transferability of the results to application-oriented ASSB cells.

These commonalities strongly indicate that the reproducible preparation of the positive electrode composite is decisive for good cell performance. It starts with the storage and handling of the materials and continues with the quality of the mixing procedure of the positive electrode materials and the SE, the homogeneous dispersion of the composite on top of the separator and the uniaxial compression profiles used.

To identify possible correlations between processing parameters and cycling performance, Fig. 3 shows the dependence of the initial specific discharge capacity, the capacity retention and total cell resistance R_{tot} , obtained from the second pretreatment charge DRT analysis²⁸

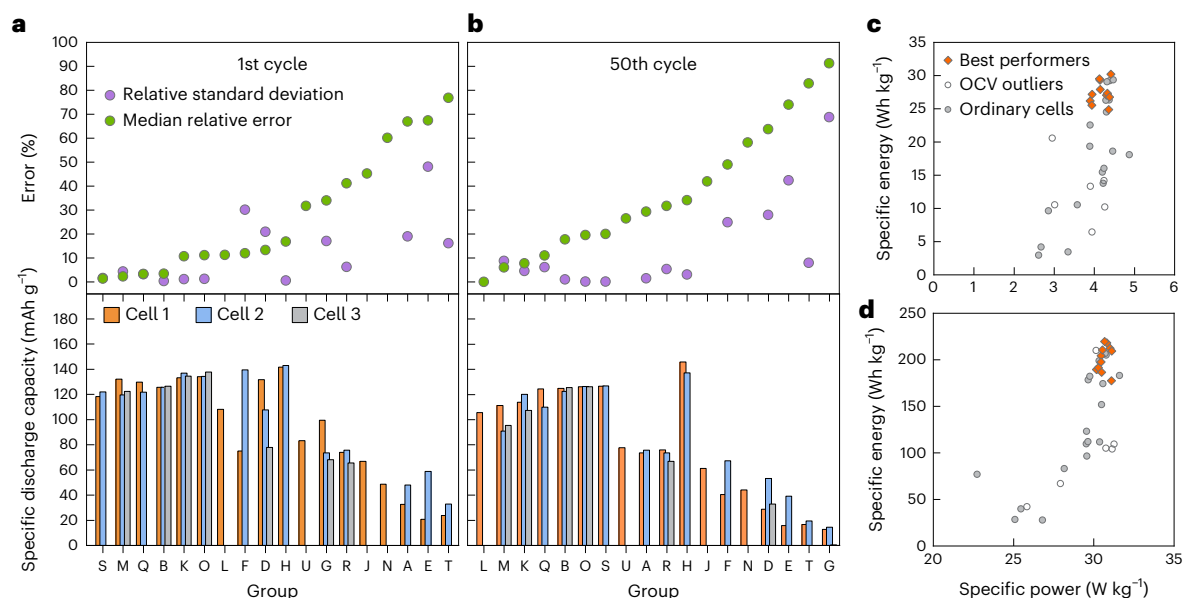


Fig. 4 | Group error and Ragone plots. **a, b**, Relative standard deviation, median relative error and specific discharge capacities in the first 0.1 C cycle (**a**) and the corresponding plots for the 50th cycle (**b**). **c, d**, Ragone plot of all prepared cells—the specific energy and power are calculated for the first 0.1 C discharge cycle

after formation (**c**)—and extrapolated Ragone plot for an optimized cell system where a 30- μm separator and 20- μm lithium-metal anode is assumed (**d**). In the Ragone plots, OCV outlier cells are shown as open circles and best performers as diamonds.

as a function of the indium content in the alloy negative electrode, the initial OCV, the cycling pressure and the initial polarization voltage. The cells classified as outliers based on the initial OCV are also shown in Fig. 3 (as open circles), except for the total cell resistances which were not determined for these outlier cells.

Starting with the proportion of indium in the $\text{In}/(\text{InLi})_x$ alloy negative electrode (Fig. 3a–c), we observe an optimum in terms of capacity and capacity retention between 60 and 75 at% of indium. At higher In and lower Li contents, cells show worse capacity retentions. In literature, similar effects are observed in rate performance tests, where worse performance is observed with lower Li contents²⁹. The spread of three *best performer* cells to high indium amounts >85 at% might originate from differences in how the alloy negative electrode was prepared, for example, if the indium or the lithium side of the alloy was facing the separator surface. The alloy preparation procedure was not reported by the groups, however, previous reports show how the amount of electrochemically accessible Li^+ and the overall cycling performance of ASSB cells can be influenced by it³⁰.

Moving to the cycling pressures (Fig. 3d–f), even though poor capacity retentions are reported for cells that implement a cycling pressure below 40 MPa, they do not correlate with attainable initial discharge capacities. R_{tot} does also not correlate with the cycling pressure, but a trend can be seen in a plot with R_0 as a function of the maximum applied pressure during assembly (Supplementary Fig. 9), where a decrease of the separator resistance R_0 with increasing maximum pressure is observed, most clearly for the *best performers*.

Regarding the OCV (Fig. 3g–i), the outliers possess either very low capacities, unusual capacity retentions or both. Conversely, high specific capacities and capacity retentions and low total cell resistances are observed at $\text{OCV} \geq 2.5 \text{ V vs Li}^+/\text{Li}$. This underlines the importance of the initial OCV measurement and that the OCV should be in the right range for a good cycling performance in cells using the electroactive materials evaluated in this study.

Finishing with the initial polarization voltages (Fig. 3j–l), a clustering of cells with high-capacity retentions and specific discharge capacities is evident for polarization voltages below 0.2 V. There is a strong linear correlation between the ‘initial’ R_{tot} (second pretreatment charge

cycle) and the initial polarization voltage. This correlation remains until the end of cycling (51st cycle R_{tot} vs final polarization voltage; Supplementary Fig. 9), demonstrating that total cell resistance and polarization voltage are consistent among each other, even though they are obtained from two different, independent techniques.

Cell reproducibility and Ragone plots

Although clear trends between the processing parameters and the electrochemical cell performance are not evident in this study, as in previous interlaboratory studies^{31–34}, these results underscore the importance of multiple measurements to validate electrochemical performance.

Figure 4a,b shows the initial specific discharge capacities of all cells along with their resulting median errors and relative standard deviations. Here the relative median errors (RMEs) and relative standard deviations (RSEs) were calculated by

$$\text{RME} = \frac{|\text{study median} - \text{group average capacity}|}{\text{study median}} \quad \text{and} \quad \text{RSE} = \frac{|\text{group standard deviation}|}{\text{group average capacity}}$$

respectively, and the data have been sorted in order of increasing relative median error. The RME is a better indicator of how each group compares to the resulting statistics of the study. If we set 10% RME as a threshold, only four groups meet this criterion in the first 0.1 C cycle (S, M, Q and B, sorted from lower to higher RME values), which includes three of the six groups chosen as best performers, all of which report the data of at least two cells. After 50 cycles, the order of the groups changes slightly, mainly due to the lower study median. Moreover, lower relative standard deviations (<10%) are obtained for the groups that report the data for three cells (in the first 0.1 C cycle: five of eight groups, namely B, H, K, O, S, Q, M and R), irrespective of where the average specific capacities of these cells lie with respect to the median for the study. Similarly, the ten groups with relative standard deviations <10% at the 50th cycle report data of at least two cells, namely groups M, K, Q, B, O, S, A, R, H, T (five of ten groups measured three cells). The standard deviations get smaller as the number of reported cells increases, decreasing from averaged 10.0 mAh g^{-1} (averaged standard deviations of the specific discharge capacities from groups reporting two cells) to 7.0 mAh g^{-1} (averaged standard deviations for groups reporting three cells). Taken together, the results of this interlaboratory

study emphasize the value of multiplicate measurements and reporting the data of each measurement for increased comparability and cell performance validation.

The Ragone plot in Fig. 4c shows the specific power and specific energy calculated from the first 0.1 C discharge cycle after the formation. For the calculation of the cell weight, only the weight of positive composite electrode, separator and In/(InLi)_x alloy was taken into account. This was done due to the unknown weights of the cell casings and the fact that these cell set-ups are often bulky and not optimized in terms of weight but of reusability. The data of group D is not included, as no voltages were reported. The specific power of all cells is similar and in a range between 2.5 W kg⁻¹ and 5 W kg⁻¹. The reasons for these small differences are the similar (dis-)charge currents used by the groups due to the prescribed positive electroactive material loading of 10 mAh cm⁻² and C rate of 0.1 C. There is a larger variation in the specific energies, ranging between 2.5 Wh kg⁻¹ and 31 Wh kg⁻¹. These differences mainly originate from the differences in the specific discharge capacity. Consequently, the *best performers* also have high specific energies.

The specific powers and energies in the present study are much lower compared to the target values of a specific energy between 250 Wh kg⁻¹ and 400 Wh kg⁻¹ and a cycling rate of 1 C (refs. 1,35). This is mainly because the lab scale cells are not optimized for high energy and power, such that the separator is very thick with around 500 μm and fast (dis-)charging, which would lead to higher specific power, was not investigated. To illustrate the influence of the thickness of separator and negative electrode on the specific energy and power, Fig. 4d shows an extrapolated Ragone plot of an optimized cell under assumption of a 30-μm thick Li₆PS₃Cl layer and a 20-μm thick lithium-metal anode (weights calculated with the theoretical densities of Li₆PS₃Cl and lithium), but with the same positive composite electrode loading and thickness as used by the groups and assuming that the resulting capacities and cell voltages of each cell do not change. The specific energies in this extrapolated system would be up to 220 Wh kg⁻¹ higher and close to the lower end of the target region. Additionally, only commercially available state-of-art materials were used, which was done to achieve better comparability and be closer to the application. Incorporating a higher-capacity NMC 811 would further increase the specific energy of the cells.

Conclusions

In the present study, the interlaboratory comparability of all-solid-state battery cycling data was investigated. Commercial NMC 622, Li₆PS₃Cl and indium foil were sent to 21 different groups. The groups were asked to assemble and cycle ASSB cells under defined conditions but using their individual cell set-ups and preparation procedures. The present study shows that the differences in cycling behaviour, specific capacities and voltages between cells prepared by different groups are huge. The initial discharge capacities at 0.1 C after a pretreatment are ranging between 23.7 mAh g⁻¹ and 143.1 mAh g⁻¹. Thus, the comparability of ASSB cell data originating from different groups and cell set-ups is limited.

To improve the comparability, we recommend that all processing and cell parameters should be carefully reported (Table 1). This study showed an extreme variation in the compression times and pressures used and the cycling pressure applied, which is expected to result in different positive composite electrode morphologies and microstructures. For good comparability, ASSB cells must be cycled at the same pressures. The use of higher stack pressures (> 40 MPa) enables cells with a better cycling performance compared to cells where lower but more application-oriented cycling pressures (0–10 MPa) are applied. Additionally, the general interlaboratory variation and the standard deviation between multiple cells of one group make it clear that publications reporting cycling data should not only report the data of one battery but at least the average and error ranges of triplicates.

Table 1 | Set of ASSB assembly parameters

Parameter	Unit
Pressures p_x , and compression times t_x used to process each cell component x (separator, positive electrode, negative electrode)	MPa and min
Compression profile at each step, that is, how fast the pressure was applied and released	
Cycling pressure p_{stack} , including if and how it was controlled during cell cycling	MPa
Atomic In-to-Li ratio in the negative alloy electrode ²⁹	at%
Positive electroactive material (CAM) loading	mg cm ⁻²
Initial open circuit voltage E_{OCV}	V vs Li ⁺ /Li
Rest time t_{rest} before cycling	min or h

Parameters that should be consistently reported together with ASSB cell cycling data.

The latter should become a standard reporting approach when discussing the effect of low-content (in)active additives (for example, polymer electrolytes, binder and so on). Otherwise, it is impossible to discriminate the effect of the additive with respect to a reference battery. Statistically, the error ranges become smaller, the more cells are prepared. With a cell failure rate of 43%, our study shows that the assembly of ASSB cells is challenging. Therefore, we recommend that the number of failed cells is reported to better assess the reproducibility and robustness of the assembly protocol.

There are several factors affecting the cell performance that we could not investigate in this study. These come into play during ASSB cell preparation, such as the (in)homogeneity of the positive composite electrode preparation via hand grinding, microstructure of each component influenced by the compression profiles, current collector surface texture, material degradation during storage and the preparation protocol of the In/(InLi)_x alloy negative electrode. Additionally, the presence of O₂, H₂O and solvents in inert atmospheres, and the control of pressure and temperature during cycling, may also impact ASSB performance. Although controlling these parameters was beyond our study's scope, our results highlight the need for further work to standardize testing, improve reproducibility and enhance the comparability of ASSB data.

In the last decade, there have been tremendous efforts in bringing the performance and understanding of ASSB to a level in which realistic application and commercialization-driven assessments of ASSB are now possible. Identifying and acknowledging the parameters that may affect comparability and benchmarking assessments are needed to provide a combined community effort for standardization to ensure the success of this technology. Further developments towards pouch cells are expected in most of the groups involved in this study. Therefore, conducting a similar study to what we report here at the pouch cell level is something we may target in a not-so-distant future.

Methods

Materials

Li₆PS₃Cl (LPSCI, MSE Supplies, 99.99%, Mesh 325, D50 ≈ 1 μm) solid electrolyte was purchased and sent to the groups as received. Single crystalline LiNi_{0.6}Mn_{0.2}Co_{0.2}O₂ (NMC 622, MSE Supplies) was used as positive electroactive material (CAM) and dried at 150 °C for 24 h under vacuum before sending. Indium foil (MaTeck, 99.999%, 100-μm thickness) was purchased, dried at 40 °C for 24 h under vacuum beforehand and used to prepare the In/(InLi)_x alloy negative electrode. Lithium metal was not sent to the groups; all groups were asked to use their own Li metal. Two hundred fifty mg of LPSCI, 100 mg of NMC 622 and three pieces of Indium foil (diameter: 12 mm, 16 mm for one group) were packed under inert argon atmosphere (O₂ < 1.0 ppm and H₂O < 0.5 ppm) and sent to each contributing group.

Powder X-ray diffraction

The phase purity of NMC 622 and in LPSCI was investigated by powder X-ray diffraction in a Stoe STADI P diffractometer (Debye–Scherrer geometry, Dectris MYTHEN 1 K detector). The powder sample of argyrodite was diluted with fumed silica to minimize the absorption. Both pristine NMC and the mixed argyrodite/silica were transferred separately into airtight glass capillaries and measured with Cu K α radiation ($\lambda = 1.54 \text{ \AA}$) with Ge 111 monochromator in a 2θ range of $10\text{--}70^\circ$. The scans were recorded with steps of 3° and a step time of 120 s.

Scanning electron microscopy

Before imaging, the LPSCI powder was surface gold sputtered with a 10 nm Au coating layer. The pristine cathode active material NMC 622 and the Au sputtered LPSCI solid electrolyte powder were fixed on a carbon pad and transferred into SEM via a vacuum-sealed sample holder. A scanning electron microscope (SEM, Carl Zeiss AURIGA field emission microscope) with a Schottky field emitter as electron source with an accelerating voltage of 3 kV was used in combination with the InLens detector.

Impedance spectroscopy

The ionic conductivity of the LPSCI solid electrolyte was determined via potentiostatic electrochemical impedance spectroscopy (PEIS) in a symmetrical ion-blocking cell set-up, using stainless-steel (SS) contacts. For the assembly, 250 mg of the LPSCI were uniaxially pressed into a pellet in a 10 mm polyether ether ketone cylinder at 380 MPa for 3 min, resulting in a pellet with $\approx 2,000\text{-}\mu\text{m}$ thickness. Two temperature-dependent PEIS measurements were performed under constant frame pressure of 60 MPa in a frequency range of 7 MHz to 100 mHz and a voltage amplitude of 10 mV. PEIS spectra were taken after each 2 h of equilibration time at the following temperatures: 10, 13, 16, 20, 25, 30, 40, 50 and 60°C .

Lithium-ion coin cell reference

Reference lithium-ion battery (LIB) coin cells were prepared to test the specific discharge capacities of the positive electrode material. For the positive electrodes, polyvinylidene difluoride (PVdF, 0.15 g, Solef 5130, Solvay) was dissolved in *N*-methyl-2-pyrrolidone (NMP, 5 g, anhydrous, 99.5%, Sigma-Aldrich). NMC 622 (4.7 g) and Super C65 (0.15 g; Imerys Graphite & Carbon) were added to the solution, resulting in a NMC 622:PVdF:Super C65 ratio of 94:3:3 wt%. The dispersion was homogenized in a Dispermat LC30 (VMA Getzmann GmbH) for 1 h at 10,000 rpm. The electrode paste was coated on a doctor blade (Zehntner GmbH) on Al foil (20 μm , Nippon foil, previously washed with ethanol) with a coating thickness of 100 μm . After drying the sheets at 80°C for 2 h, calendaring was performed with 5- μm gap size. The positive electrodes were punched (diameter: 14 mm) and dried for 16 h at 120°C under vacuum. Two-electrode coin cells (CR2032, Hohsen Corporation) were assembled with a polymer membrane separator (diameter: 16 mm, Celgard 2500, 25 μm , Celgard) and Li metal as negative electrode (diameter: 15 mm, 500 μm , $\geq 99.9\%$, China Energy Lithium (CEL Co.)). As electrolyte, 1 M LiPF $_6$ in 3:7 vol% EC:EMC (35 μl ; battery line HTS; battery grade) was used. The two spacers possessed a thickness of 0.5 mm and 1 mm, respectively. The LIBs exhibited a CAM loading of 6 mg cm^{-2} , the cycling procedure was the same as for the ASSBs, but without the PEIS measurements.

Solid-state battery assembly

The groups were asked to prepare three all-solid-state battery (ASSB) cells and cycle them, with the following specifications: the positive composite electrode (CC) should be prepared by mixing of NMC 622:LPSCI in a ratio $m(\text{CAM}):m(\text{SE}) = 70:30$ for up to 15 min with mortar and pestle. The target positive electroactive material loading should be 10 mg cm^{-2} and the separator should consist of pristine LPSCI with a loading of 75 mg cm^{-2} and a thickness of 300–400 μm . The In/(InLi) $_x$

($x \approx 0.3$) negative electrode should be prepared by pressing the provided In foil and Li metal from the specific group to obtain a total negative alloy thickness of $\approx 100 \mu\text{m}$.

ASSB cell cycling

Before cycling, the OCV should be measured and a potentiostatic electrochemical impedance (PEIS) measurement at OCV should be performed in a frequency range 7 MHz (or highest frequency possible) to 100 mHz with a voltage amplitude of 10 mV and 10 data points per decade being taken. These parameters are the measurement settings for all further PEIS measurements. The cycling should be performed with symmetrical constant current charging and discharging, assuming 200 mAh g^{-1} as theoretical capacity for the CAM. As voltage window, 3.0 V to 4.3 V vs Li $^+$ /Li (assuming that 0 V vs Li $^+$ /(In–InLi) = 0.62 V vs Li $^+$ /Li) should be used. The cells should undergo a pretreatment process of two cycles at 0.05 C. After the first charge and a 1 h OCV step, a PEIS should be performed. The first discharge should be followed by another 1 h OCV step and PEIS measurement. After repeating this procedure of a charge and discharge cycle including a PEIS measurement for a second 0.05 C charge and discharge cycle, cycling should be performed at 0.1 C for 50 cycles with a rest step of 5 min between each charge/discharge step. After cycling, a PEIS measurement in the charged and discharged state should be measured after each a 1 h OCV step. Supplementary Figs. 11–27 show the specific charge/discharge curves of all cells groupwise. For each cell, the cycles 1, 2, 10, 20, 30, 40 and 50 are shown, assuming cycle 1 as the first 0.1 C cycle after the pretreatment. Group D is not shown, as no voltages were reported.

Cycling data evaluation

Each group sent the raw data files containing time, voltage, current and cycle number. The specific (dis-) charge capacities Q_{spec} were calculated from these values:

$$Q_{\text{spec}} = \frac{It}{m_{\text{CAM}}} \quad (1)$$

with I being the applied current, t the time the current was applied in the according (dis-)charge step and m_{CAM} the mass of the CAM.

The polarization voltage ΔV was calculated from the difference of the average charge and discharge voltages U_{average} :

$$\Delta V = U_{\text{average,charge}} - U_{\text{average,discharge}} \quad (2)$$

The accumulated irreversible capacity Q_{AIC} is calculated from the sum of the irreversible capacities Q_{irr} of the 0.1 C cycles:

$$Q_{\text{irr}} = Q_{\text{charge}} - Q_{\text{discharge}} \quad (3)$$

$$Q_{\text{AIC}} = \sum_{n=1}^{n=x} Q_{\text{irr}}(n) \quad (4)$$

The specific energy densities E_{spec} were calculated from the second 0.05 C pretreatment discharge cycle and the first 0.1 C discharge cycle after the pretreatment:

$$E_{\text{spec}} = \frac{QU_{\text{average}}}{m_{\text{cell}}} = \frac{QU_{\text{average}}}{m_{\text{Li}} + m_{\text{In}} + m_{\text{separator}} + m_{\text{cathode composite}}} \quad (5)$$

with Q being the specific discharge capacity, U_{average} the average discharge voltage and m_{cell} the sum of all materials in the ASSB cell. The weight of the battery cell casing was not considered, as different lab scale cells set-ups with unknown weights were used by the different groups.

The specific power P_{spec} was calculated from the second 0.05 C pretreatment discharge cycle and the first 0.1 C discharge cycle as well:

$$P_{\text{spec}} = \frac{IU_{\text{average}}}{m_{\text{cell}}} \quad (6)$$

For the extrapolated Ragone plot, a very thin electrolyte separator (30 μm) and a thin lithium anode (20 μm) were assumed. The weights of these thin LPSCl or lithium films were calculated from the group-specific cell area A_{cell} and the theoretical densities of LPSCl or lithium, respectively.

$$m_{\text{Li}} = A_{\text{cell}} \times 0.002 \text{ cm} \times 0.534 \text{ g cm}^{-3}$$

$$m_{\text{LPSCl}} = A_{\text{cell}} \times 0.003 \text{ cm} \times 1.87 \text{ g cm}^{-3}$$

The extrapolated specific power and specific energy were calculated with equations (5) and (6) using the assumed weights m_{Li} and m_{LPSCl} , the experimental $m_{\text{Cathode composite}}$ and the experimental cycling data.

Impedance data evaluation

Supplementary Fig. 10 shows the data processing and analysis steps for the impedance spectrum of cell 1 of group K as an example. First, the impedance data provided by each group is validated regarding the LTI criteria, namely linearity, stationarity and time invariance. This is achieved through the utilization of two state-of-the-art methods: the extended Kramers–Kronig test³⁶, which is based on the Kramers–Kronig relation and the Z-HIT algorithm²⁸, which is based on the Hilbert transform applied to two pole systems. Both methods can detect violations of the assumed criteria by examining the noise (statistical error) and the mean (systematic error) of the residuals. According to the results presented in Supplementary Fig. 10, both methods indicate decreasing quality for frequencies higher than 500 kHz, because of which the spectra were truncated for $f \geq 500$ kHz.

Subsequently, the impedance data is transformed into the time domain by the distribution of relaxation times method (DRT) to enhance the spectral resolution and allow the separation of characteristic electrochemical processes and their polarization contribution in the spectrum. This is achieved by calculating the distribution function of a specified kernel function. For purely resistive-capacitive spectra, the kernel function is equal to the transfer function of a circuit of a resistor (R) and capacitor (C) connected in parallel (RC circuit) with a time constant and a polarization, resulting in a distribution of polarization versus time constants. To allow the analysis of more arbitrary spectra containing an ohmic offset, inductive and capacitive features, Hahn et al.³⁷ proposed the addition of lumped serial elements to the DRT with the extended DRT (eDRT). Analogous to the resistive-capacitive distribution function, Danzer²⁷ introduced a second distribution function for resistive-inductive features in the spectrum with the generalized DRT (gDRT), which is used here for the further analysis. It should be noted that the resulting distribution is discrete for logarithmically spaced time constants, and that it is plotted with a continuous line for visual purposes.

The used method to obtain the distribution function is based on a Tikhonov L2-regularization based algorithm, which requires the careful selection of the regularization parameter λ . The regularization helps to find a unique solution but also acts as smoothing filter. The L-curve method³⁸ can be used to find a suitable range for a mathematical optimal regularization parameter. However, as this dataset is very heterogeneous regarding the absolute polarization, the measurement equipment and thus the signal-to-noise ratio, it is difficult to find one unique regularization parameter that fits all measurements. Therefore, the regularization parameter is primarily based on the mathematical optimum but changed in favour of comparable distribution functions when needed. An overview is provided in Supplementary Table 22. Supplementary Fig. 10 shows an example of the solution based on the gDRT method. The range of time constants is extended by one decade in each direction to reduce boundary effects, and the number of time constants is three times the number of measurement points. The shown distribution function is composed of the sum of the resistive-capacitive and the negative resistive-inductive distribution. Due to the mainly

resistive-capacitive nature of the investigated spectra, no inductive and resistive-inductive features can be observed in the results of the gDRT analysis. The lumped elements R_0 , C_0 and L_0 are obtained directly from the gDRT, whereas the total polarization R_{tot} is calculated by the sum of polarization for the resistive-capacitive distribution function:

$$R_{\text{tot}} = \sum h_{\text{RC}} \quad (7)$$

Supplementary Figs. 29–43 show the impedance and calculated distribution functions in groups. For each group and cell, the impedance of the first, second and 51st charging cycle is used. For the DRT, the obtained lumped serial elements and total polarization are summarized in Supplementary Table 22 and the corresponding figure.

Data availability

All data used in this study are included in the paper and its Supplementary Information. Source data are provided with this paper.

Code availability

The code for the Kramers–Kronig validation and the distribution of relaxation times method is part of the EC-Idea software toolbox developed at the Chair of Electrical Energy Systems at the University of Bayreuth and is available online at <https://www.ees.uni-bayreuth.de/en/ec-idea/index.html>.

References

1. Randau, S. et al. Benchmarking the performance of all-solid-state lithium batteries. *Nat. Energy* **5**, 259–270 (2020).
2. Grandjean, M. et al. Low pressure cycling of solid state Li-ion pouch cells based on NMC–sulfide–nanosilicon chemistry. *J. Power Sources* **585**, 233646 (2023).
3. Kim, M.-J. et al. Facile fabrication of solution-processed solid-electrolytes for high-energy-density all-solid-state-batteries by enhanced interfacial contact. *Sci. Rep.* **10**, 11923 (2020).
4. Quemin, E. et al. An advanced cell for measuring in situ electronic conductivity evolutions in all-solid-state battery composites. *Adv. Energy Mater.* <https://doi.org/10.1002/aeam.202301105> (2023).
5. Quemin, E. et al. Decoupling parasitic reactions at the positive electrode interfaces in argyrodite-based systems. *ACS Appl. Mater. Interfaces* **14**, 49284–49294 (2022).
6. Ruhl, J., Riegger, L. M., Ghidui, M. & Zeier, W. G. Impact of solvent treatment of the superionic argyrodite $\text{Li}_6\text{PS}_5\text{Cl}$ on solid-state battery performance. *Adv. Energy Sustain. Res.* <https://doi.org/10.1002/aesr.202000077> (2021).
7. Walther, F. et al. Visualization of the interfacial decomposition of composite cathodes in argyrodite-based all-solid-state batteries using time-of-flight secondary-ion mass spectrometry. *Chem. Mater.* **31**, 3745–3755 (2019).
8. Choi, S. et al. Application of rod-like $\text{Li}_6\text{PS}_5\text{Cl}$ directly synthesized by a liquid phase process to sheet-type electrodes for all-solid-state lithium batteries. *J. Electrochem. Soc.* **166**, A5193–A5200 (2019).
9. Sun, X. et al. A bifunctional chemomechanics strategy to suppress electrochemo-mechanical failure of Ni-rich cathodes for all-solid-state lithium batteries. *ACS Appl. Mater. Interfaces* **14**, 17674–17681 (2022).
10. Minnmann, P., Quillman, L., Burkhardt, S., Richter, F. H. & Janek, J. Editors' choice—quantifying the impact of charge transport bottlenecks in composite cathodes of all-solid-state batteries. *J. Electrochem. Soc.* **168**, 40537 (2021).
11. Doux, J.-M. et al. Pressure effects on sulfide electrolytes for all solid-state batteries. *J. Mater. Chem. A* **8**, 5049–5055 (2020).
12. Gittins, J. W. et al. Interlaboratory study assessing the analysis of supercapacitor electrochemistry data. *J. Power Sources* **585**, 233637 (2023).

- Cronau, M., Szabo, M., König, C., Wassermann, T. B. & Roling, B. How to measure a reliable ionic conductivity? the stack pressure dilemma of microcrystalline sulfide-based solid electrolytes. *ACS Energy Lett.* **6**, 3072–3077 (2021).
- Perrenot, P. et al. Room-temperature sintering of amorphous thiophosphate solid electrolyte (Li₃PS₄): coupling morphological evolution to electrochemical properties. *Adv. Funct. Mater.* <https://doi.org/10.1002/adfm.202310739> (2024).
- Perrenot, P., Bayle-Guillemaud, P. & Villevieille, C. Composite electrode (LiNi_{0.6}Mn_{0.2}Co_{0.2}O₂) engineering for thiophosphate solid-state batteries: morphological evolution and electrochemical properties. *ACS Energy Lett.* **8**, 4957–4965 (2023).
- Bielefeld, A., Weber, D. A. & Janek, J. Microstructural modeling of composite cathodes for all-solid-state batteries. *J. Phys. Chem. C*. **123**, 1626–1634 (2019).
- Del Olmo, D., Pavelka, M. & Kosek, J. Open-circuit voltage comes from non-equilibrium thermodynamics. *J. Non-Equilib. Thermodyn.* **46**, 91–108 (2021).
- Liu, C., Neale, Z. G. & Cao, G. Understanding electrochemical potentials of cathode materials in rechargeable batteries. *Mater. Today* **19**, 109–123 (2016).
- Schmidt, J. P., Tran, H. Y., Richter, J., Ivers-Tiffée, E. & Wohlfahrt-Mehrens, M. Analysis and prediction of the open circuit potential of lithium-ion cells. *J. Power Sources* **239**, 696–704 (2013).
- Cui, H. et al. Operando monitoring of the open circuit voltage during electrolyte filling ensures high performance of lithium-ion batteries. *Nano Energy* **104**, 107874 (2022).
- Santhosha, A. L., Medenbach, L., Buchheim, J. R. & Adelhelm, P. The indium–lithium electrode in solid-state lithium-ion batteries: phase formation, redox potentials, and interface stability. *Batteries Supercaps* **2**, 524–529 (2019).
- Koerver, R. et al. Capacity fade in solid-state batteries: interphase formation and chemomechanical processes in nickel-rich layered oxide cathodes and lithium thiophosphate solid electrolytes. *Chem. Mater.* **29**, 5574–5582 (2017).
- Kasnatscheew, J. et al. The truth about the 1st cycle Coulombic efficiency of LiNi_{1/3}Co_{1/3}Mn_{1/3}O₂ (NCM) cathodes. *Phys. Chem. Chem. Phys.* **18**, 3956–3965 (2016).
- Kitsche, D. et al. High performance all-solid-state batteries with a Ni-rich NCM cathode coated by atomic layer deposition and lithium thiophosphate solid electrolyte. *ACS Appl. Energy Mater.* **4**, 7338–7345 (2021).
- Reissig, F. et al. Investigation of lithium polyacrylate binders for aqueous processing of Ni-rich lithium layered oxide cathodes for lithium-ion batteries. *ChemSusChem* **15**, e202200401 (2022).
- Weber, R., Louli, A. J., Plucknett, K. P. & Dahn, J. R. Resistance growth in lithium-ion pouch cells with LiNi_{0.80}Co_{0.15}Al_{0.05}O₂ positive electrodes and proposed mechanism for voltage dependent charge-transfer resistance. *J. Electrochem. Soc.* **166**, A1779–A1784 (2019).
- Danzer, M. A. Generalized distribution of relaxation times analysis for the characterization of impedance spectra. *Batteries* **5**, 53 (2019).
- Plank, C. et al. A review on the distribution of relaxation times analysis: a powerful tool for process identification of electrochemical systems. *J. Power Sources* **594**, 233845 (2024).
- Yanev, S. et al. Editors' choice—alleviating the kinetic limitations of the Li-In alloy anode in all-solid-state batteries. *J. Electrochem. Soc.* **171**, 20512 (2024).
- Sedlmeier, C., Schuster, R., Schramm, C. & Gasteiger, H. A. A micro-reference electrode for electrode-resolved impedance and potential measurements in all-solid-state battery pouch cells and its application to the study of indium-lithium anodes. *J. Electrochem. Soc.* **170**, 30536 (2023).
- Ohno, S. et al. How certain are the reported ionic conductivities of thiophosphate-based solid electrolytes? An interlaboratory study. *ACS Energy Lett.* **5**, 910–915 (2020).
- Ehelebe, K. et al. Benchmarking fuel cell electrocatalysts using gas diffusion electrodes: inter-lab comparison and best practices. *ACS Energy Lett.* **7**, 816–826 (2022).
- Hill, R. J. Rietveld refinement round robin. I. Analysis of standard X-ray and neutron data for PbSO₄. *J. Appl. Crystallogr.* **25**, 589–610 (1992).
- Tesch, M. F., Neugebauer, S., Narangoda, P. V., Schlögl, R. & Mechler, A. K. The rotating disc electrode: measurement protocols and reproducibility in the evaluation of catalysts for the oxygen evolution reaction. *Energy Adv.* **2**, 1823–1830 (2023).
- van Noorden, R. The rechargeable revolution: a better battery. *Nature* **507**, 26–28 (2014).
- Plank, C., Ruther, T. & Danzer, M. A. Detection of non-linearity and non-stationarity in impedance spectra using an extended Kramers–Kronig test without overfitting. In *2022 International Workshop on Impedance Spectroscopy (IWIS) 1–6* (IEEE, 2022); <https://doi.org/10.1109/IWIS57888.2022.9975131>
- Hahn, M. et al. Investigating solid polymer and ceramic electrolytes for lithium-ion batteries by means of an extended distribution of relaxation times analysis. *Electrochim. Acta* **344**, 136060 (2020).
- Paul, T., Chi, P. W., Wu, P. M. & Wu, M. K. Computation of distribution of relaxation times by Tikhonov regularization for Li ion batteries: usage of L-curve method. *Sci. Rep.* **11**, 12624 (2021).

Acknowledgements

The S.P. and N.M.V.-B. acknowledge the FESTBATT Cluster of Competence funded by the Bundesministerium für Bildung und Forschung (BMBF; project 13XP0428A) for support to coordinate this study. The coordinating group would like to thank all participating groups for agreeing to make these data fully accessible.

Author contributions

The study was jointly designed by S.P. and N.M.V.-B. The coordinating group (S.P., E.N., F.K., H.M.W., J.F.T. and N.M.V.-B.) were responsible for sourcing all materials, initial material characterization, sample preparation, shipping of materials, data collection and cycling data analysis. Impedance data analysis was done by C.P. and M.D. All authors (S.P., E.N., F.K., H.M.W., J.F.T., Z.C., A.F.-M., A.G., M.G., S.-Y.H., M.-T.H., M.-G.J., D.H., J.S.K. T.K., B.L., P.M., V.M., K.M., D.L.N., F.O., F.P., C.P., M.R., S.E.S., E.S., R.S., D.S.-J., Y.S., B.S.V., R.Z., H.Z., P.A., T.B., P.G.B., M.D., M.E.K. H.G., K.B.H., A.H., F.H., J.J., Y.S.J., M.T.M., Y.S.M., P.P.M., S.O., B.R., A.S., J.S., X.S., C.V., M.W., W.G.Z. and N.M. V.-B.) contributed to writing the paper.

Funding

Open access funding provided by Universität Bayreuth.

Competing interests

The authors declare no competing interests.

Additional information

Supplementary information The online version contains supplementary material available at <https://doi.org/10.1038/s41560-024-01634-3>.

Correspondence and requests for materials should be addressed to Nella M. Vargas-Barbosa.

Peer review information *Nature Energy* thanks Hong Li and the other, anonymous, reviewer(s) for their contribution to the peer review of this work.

Reprints and permissions information is available at www.nature.com/reprints.

Publisher's note Springer Nature remains neutral with regard to jurisdictional claims in published maps and institutional affiliations.

Open Access This article is licensed under a Creative Commons Attribution 4.0 International License, which permits use, sharing, adaptation, distribution and reproduction in any medium or format, as long as you give appropriate credit to the original author(s) and the

source, provide a link to the Creative Commons licence, and indicate if changes were made. The images or other third party material in this article are included in the article's Creative Commons licence, unless indicated otherwise in a credit line to the material. If material is not included in the article's Creative Commons licence and your intended use is not permitted by statutory regulation or exceeds the permitted use, you will need to obtain permission directly from the copyright holder. To view a copy of this licence, visit <http://creativecommons.org/licenses/by/4.0/>.

© The Author(s) 2024

¹Institute of Energy Materials and Devices (IMD), IMD-4: Helmholtz-Institut Münster, Forschungszentrum Jülich, Münster, Germany. ²Institute of Inorganic and Analytical Chemistry, University of Münster, Münster, Germany. ³International Graduate School for Battery Chemistry, Characterization, Analysis, Recycling and Application (BACCARA), University of Münster, Münster, Germany. ⁴University of Münster, MEET Battery Research Center, Institute of Physical Chemistry, Münster, Germany. ⁵Institute of Business Administration at the Department of Chemistry and Pharmacy, University of Münster, Münster, Germany. ⁶Storage of Electrochemical Energy, Department of Radiation Science and Technology, Faculty of Applied Sciences, Delft University of Technology, Delft, The Netherlands. ⁷Université Grenoble Alpes, Université Savoie Mont Blanc, CNRS, Grenoble INP, LEPMI, Grenoble, France. ⁸Fraunhofer Institute for Manufacturing and Advanced Materials IFAM, Bremen, Germany. ⁹Materials Science and Engineering Program, University of California San Diego, La Jolla, CA, USA. ¹⁰School of Mechanical Engineering, Purdue University, West Lafayette, IN, USA. ¹¹Department of Mechanical and Aerospace Engineering and the Andlinger Center for Energy and the Environment, Princeton, NJ, USA. ¹²Department of Applied Chemistry, Graduate School of Engineering, Osaka Metropolitan University, Osaka, Japan. ¹³Department of Chemical and Biomolecular Engineering, Yonsei University, Seoul, Korea. ¹⁴Chair for Technical Electrochemistry, Department of Chemistry and Catalysis Research Center, Technische Universität München, Garching, Germany. ¹⁵TUMint-Energy Research GmbH, Munich, Germany. ¹⁶Electrochemistry Laboratory, Paul Scherrer Institut, Villigen, Switzerland. ¹⁷Institute of Physical Chemistry and Center for Materials Research, Justus Liebig University Giessen, Giessen, Germany. ¹⁸Department of Chemistry, Philipps-Universität Marburg, Marburg, Germany. ¹⁹School of Materials Science and Engineering, Georgia Institute of Technology, Atlanta, GA, USA. ²⁰Institut für Chemie, Humboldt Universität zu Berlin, Berlin, Germany. ²¹Joint Research Group Operando Battery Analysis (CE-GOBA), Helmholtz-Zentrum Berlin, Berlin, Germany. ²²Chair of Electrical Energy Systems, University of Bayreuth, Bayreuth, Germany. ²³Bavarian Center for Battery Technology, University of Bayreuth, Bayreuth, Germany. ²⁴Department of Surface and Battery Technology, Fraunhofer Institute for Material and Beam Technology (IWS), Dresden, Germany. ²⁵Department of Inorganic Chemistry, Technical University Dresden, Dresden, Germany. ²⁶George W. Woodruff School of Mechanical Engineering, Georgia Institute of Technology, Atlanta, GA, USA. ²⁷Department of Materials, University of Oxford, Oxford, UK. ²⁸School of Metallurgy and Materials, University of Birmingham, Birmingham, UK. ²⁹Department of Mechanical and Materials Engineering, University of Western Ontario, London, Ontario, Canada. ³⁰Institute of Nanotechnology, Karlsruhe Institute of Technology (KIT), Karlsruhe, Germany. ³¹Department of Applied Chemistry, Graduate School of Engineering, Kyushu University, Fukuoka, Japan. ³²Department of Chemistry, University of Oxford, Oxford, UK. ³³Department of NanoEngineering, University of California San Diego, La Jolla, CA, USA. ³⁴Pritzker School of Molecular Engineering, University of Chicago, Chicago, IL, USA. ³⁵Institute of Multidisciplinary Research for Advanced Materials, Tohoku University, Sendai, Japan. ³⁶Chair of Electrochemistry, University of Bayreuth, Bayreuth, Germany. ✉e-mail: n.vargas-barbosa@uni-bayreuth.de